MTLA 44 (2025) 102554

Contents lists available at ScienceDirect

Materialia

journal homepage: www.elsevier.com/locate/mtla

Full Length Article

Phase decomposition in the equiatomic CoCrNi alloy

Sakshi Bajpai [a], Xin Wang [b], Bijun Xie [a], Hangman Chen [a], Jize Zhang [c], Calvin Belcher [a], Benjamin MacDonald [a], Julia Ivanisenko [d], Yu Zhong [c], Penghui Cao [a], Enrique J. Lavernia [a,e], Diran Apelian [a,*]

[a] University of California, Irvine, Department of Materials Science and Engineering, Irvine, CA, United States
[b] University of Alabama, Tuscaloosa, Department of Metallurgical and Materials Engineering, Tuscaloosa, AL, United States
[c] Worcester Polytechnic Institute, Mechanical & Materials Engineering, MA, United States
[d] Institute for Nanotechnology, Karlsruhe Institute for Technology, Germany
[e] Texas A&M University, Department of Materials Science and Engineering, TX, United States

ARTICLE INFO

Keywords:
High pressure torsion
Phase decomposition
Equiatomic CoCrNi

ABSTRACT

Complex, concentrated alloys (CCAs) are composed of multiple principal elements in significant proportions and have attracted substantial interest due to their distinctive properties. It was initially thought that CCAs formed primarily as single-phase structures; however, subsequent research has revealed that CCAs may undergo phase decomposition when subjected to intermediate temperatures over extended durations. This study investigates the phase stability of equiatomic CoCrNi alloy, commonly recognized as a single-phase face-centered cubic (FCC) material. The alloy was subjected to severe plastic deformation, resulting in a high density of grain boundaries and deformation-induced structures. Guided by the calculation of phase diagrams (CALPHAD) predictions, prolonged annealing at a selected temperature was conducted to evaluate its phase stability. Microstructural characterization from the micro- to atomic-scale revealed that the FCC matrix undergoes structural decomposition into an HCP phase, accompanied by elemental partitioning within this phase. Transmission electron microscopy confirmed the presence of the HCP phase, while high-throughput CALPHAD and hybrid Monte Carlo/Molecular Dynamics simulations provided mechanistic insights into its formation. The emergence of this HCP phase, and the associated redistribution of elements, explains the observed differences in phase constitution compared to previously studied alloys. These findings highlight the critical role of processing-dependent phase evolution and elemental partitioning in dictating the performance of complex concentrated alloys (CCAs), thereby influencing their mechanical properties and long-term reliability in demanding applications.

1. Introduction

The emergence of high entropy alloys (HEAs) in 2004 highlighted a new class of materials characterized by multiple principal elements. The initial definitions of HEAs involved alloys of more than 5 elements in equiatomic ratios. Such a composition was thought to have high configurational entropy, leading to a disordered, single-phase microstructure. However, as the importance of the enthalpic contribution in phase formation was realized [1], it became clear that multiple phases can exist in HEAs. The research slowly progressed towards exploring non-dilute compositional alloy design spaces beyond focusing on strict definitions based on several elements and phases. Other terms, such as complex concentrated alloys (CCAs) and multiple principal element alloys (MPEAs), were even coined to reflect the idea of exploring the central region of compositional space [2–5].

One of the most well-researched CCAs is the equiatomic CoCrFeMnNi alloy, widely described as the Cantor alloy [6]. This alloy is well known for its excellent mechanical behavior at room and cryogenic temperatures [7,8]. In numerous initial studies, the Cantor alloy was considered to consist of a stable single-phase face-centered cubic (FCC) structure. However, Otto et al. [9] demonstrated that when the Cantor alloy was annealed at an intermediate temperature (500–700 °C) for an extended period, the FCC phase decomposed into secondary phases like Cr-rich σ, B2 FeCo, and L10 NiMn phases. This study was done on a homogenized and undeformed alloy. It was also found that severe plastic deformation processing like high-pressure torsion (HPT) further accelerates the kinetics of the decomposition of the FCC phase in the Cantor alloy by providing a higher density of grain boundaries as nucleation sites for the

* Corresponding author.
E-mail address: dapelian@uci.edu (D. Apelian).

https://doi.org/10.1016/j.mtla.2025.102554
Received 18 May 2025; Accepted 14 September 2025
Available online 17 September 2025

other phases. In one such case, Cr-rich σ phase precipitated in a Cantor alloy processed by high-pressure torsion and annealed at 600 °C for 60 min [10]. Similar phase decomposition is also exhibited by other CCAs, listed in Table 1.

These findings support the hypothesis that processing pathways and heat treatment conditions influence the stability of these alloys with such complex compositions. A commonly considered stable phase might be a metastable phase and may decompose when given sufficient thermodynamic and kinetic drive. Unlike conventional alloys, the complex nature of CCAs makes it challenging to predict whether a particular phase will decompose. Over the years, thermodynamic data have improved to predict phase evolution in these systems better. However, in most cases, predictions are based on ideal/equilibrium conditions, which might differ significantly from practical conditions. Hence, in the case of CCAs, it is essential to be cautious while considering phase stability. These alloys with many constituents that exhibit a single solution phase near the alloy's melting point can decompose at intermediate temperatures based on the system's free energy. Such phase decomposition will also affect the mechanical properties of the alloy.

In some cases, phase decomposition can lead to an increase in strength with a loss in ductility [11,12]; in others, it can lead to a reduction in strength [13–16]. The actual effect depends on the size, shape, coherency, and amount of phase formed. If CCAs are to be considered for structural applications, it is essential to understand any phase decomposition that might occur at given operating temperatures. Long-term annealing treatments and computational studies are being used to understand the phase stability of CCAs.

The alloy of interest for this work is the equiatomic CoCrNi alloy. It is considered a subset of the equiatomic Cantor alloy, which is known for impressive tensile strength (greater than 1 GPa) and toughness(K_{JIc} fracture-toughness values above 200 MPa $m^{1/2}$) [30], even superior to the Cantor alloy [31,32]. In general, CoCrNi is considered a single-phase FCC alloy. In the past few years, it has been shown that the alloy exhibits local chemical ordering, which is a preferential arrangement of atoms with first and second nearest neighbors. This ordering is a very localized phenomenon and not a secondary phase formation. However, in a few studies focusing on severe plastic deformation processing of the CoCrNi alloy, a minority phase has been reported. Schuh et al. [33] observed a minority HCP phase formed in the alloy after high-pressure torsion and subsequent long-term annealing. The HCP phase's formation was attributed to Co's tendency to segregate at stacking faults. The precipitates formed in this case are spherical. In another study by Deng et al. [34], the formation of ε-martensite type minority phase was reported in CoCrNi alloy when annealed at 500 °C and 600 °C for one hour after equal-channel angular pressing (ECAP). A couple of other studies that involved powder metallurgical processing of the CoCrNi alloy report different phase formations. As an example, Moravcik et al. [35] report the presence of an entirely Cr-rich BCC phase at the grain boundaries in a spark plasma sintered CoCrNi alloy with depletion of Co and Cr. In related studies, Cao et al. [36] report the formation of the HCP Co phase in a DC magnetron sputter CoCrNi coating and they rationalize the origin of the HCP phase to the presence of excess Co (by ~3 at%) during the coating deposition. However, it cannot be considered a phase decomposition as the excess Co was related to deposition conditions rather than any microstructural changes in the coating.

Based on the prior published results described above, one may arrive at the following three observations. First, the single-phase FCC CoCrNi alloy can indeed decompose into secondary phases. Second, the type of phases that form is affected by the conditions used during processing and the type of processing used. Third, there is a lack of fundamental information on the underlying mechanism(s) that govern the formation of secondary phases in single-phase CoCrNi. For example, it is not evident why an HCP phase forms under certain conditions instead of the thermodynamically stable sigma phase (as shown in Fig. 1a).

Table 1
Reported phase decomposition in CCAs.

Alloy	Synthesis/ Processing	Initial phase	Annealing parameters	Secondary phase after annealing
$Al_{0.5}CoCrCuFeNi$ [17]	Arc melting + Rolling	Two FCC phases	700 °C	Two FCC + two BCC + σ-phase
			900 °C	Two FCC + two BCC phases
			1100 °C	Two FCC phases, with high Cu content
$CuCr_2Fe_2NiMn$ [18]	Arc melting	FCC + BCC phases	600 °C - 800 °C	Cu-rich FCC + (Cr, Fe, Ni)-rich FCC+ ρ phases
			1100 °C	Cu-rich FCC + (Cr, Fe, Ni)-rich FCC phases
CoCrFeNi [19]	Arc melting	Fcc phase	750 °C, 800 h	(Potential)fcc phase precipitation similar to GP zones in Al alloys
Al1.5CrFeMnTi [20]	Arc melting	$L2_1$ + BCC + C14 phases	750 °C / 850 °C / 1200 °C, 168 h and 1000 °C, 504 h	$L2_1$ phase varies with the annealing conditions
$Al_{0.3}CoCrFeNi$ [21]	Arc melting	FCC phase	620 °C for 50 h	FCC + B2 + sigma phases
$Al_{0.5}CoCrFeMo_{0.1}Ni$ [22]	Arc melting	FCC + BCC/B2	800 °C -1000 °C ,10 h	FCC + BCC/B2 + σ phases
			1100 °C -1200 °C ,10 h	FCC + BCC/B2 phases
$Al_{0.5}CoCrFeMo_{0.2\text{-}0.3}Ni$ [22]	Arc melting	FCC + BCC/B2 + σ	1100 °C, 10 h	FCC + BCC/B2 phases
$Co_{0.18}Cr_{0.20}Fe_{0.24}Ni_{0.19}Ti_{0.19}$ [23]	HEBM**	FCC + BCC phases	600 °C -1000 °C, 204 days	Two FCC phases + ~$Co_{0.2}Ni_{0.5}Ti_{0.3}$ intermetallic
AlCoFeMnNi [24]	Arc melting	B2 phase	1050 °C, 50 h	Disordered BCC + FCC phases
ZrTiHfCuNiFe [25]	Arc melting	B2 phase	750 °C, 1000 h	B2 + HCP phases
AlCoCuNiZn [26]	Ball milling + SPS**	β FCC phase	400 °C -600 °C, 48 h	ϒ FCC* + $L1_2$ phases
AlCoCrFeNiTi [27]	Mechanical alloying	BCC +HCP (WC contamination)	DSC to 1000 °C	B2 + HCP
TiZrNbHfTa [16]	Arc melting + HPT**	BCC phase	500 °C, 1 h and 100 h	BCC + HCP phases
			800 °C, 1 h	Two BCC + HCP phases
			900 °C, 1 h	Two BCC phases
$Hf_{0.5}Nb_{0.5}Ta_{0.5}Ti_{1.5}Zr$ [28]	Arc melting+ suction- cast+ HA**+ RA**	BCC phase	500 °C, 14 days	Two BCC + HCP phases
			700 °C, 14 days	Two BCC phases
			900 °C, 14 days	Single BCC phase
AlTiVNb [29]	Arc melting + HPT**	BCC phase	700 °C - 900 °C, 1 h	BCC+ Nb_2Al and Ti_3Al intermetallic phases

*The β and ϒ FCC have only a slight difference in lattice parameter.
**SPS: Spark Plasma Sintering,
HEBM: High Energy Ball Milling,
HPT: High-Pressure Torsion
HA: Homogenization Annealing
RA: Recrystallization Annealing.

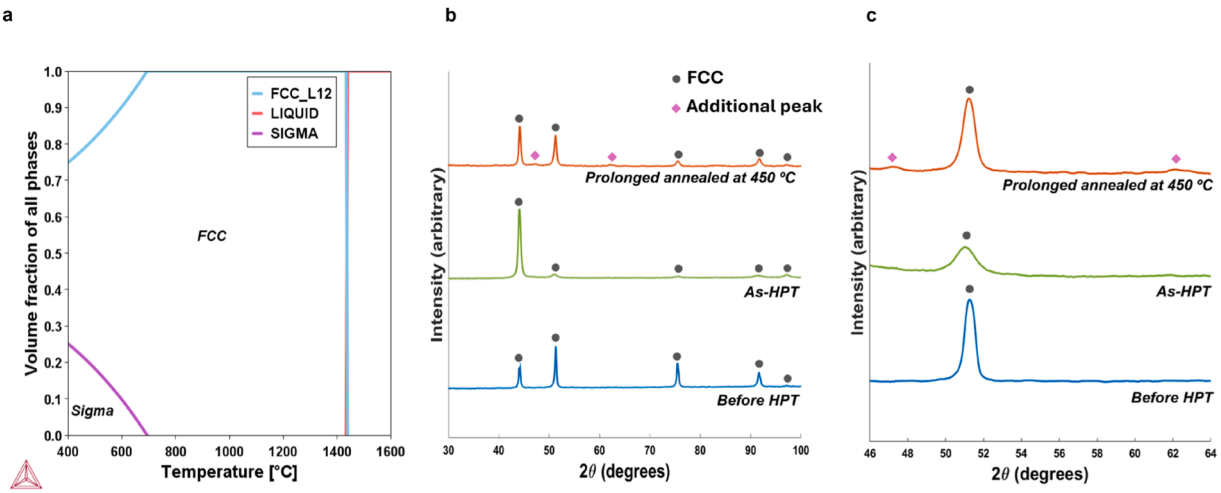

Fig. 1. (a) Phase stability diagram calculated using TCHEA6 database in ThermoCalc (b) XRD pattern of the CoCrNi alloy before HPT, in the as-HPT state, and long-term annealed state. (c)A zoomed-in view of the XRD pattern of the alloys in the same three states.

Motivated by the above discussion, the scientific objective of this study is to provide fundamental insight into the possible mechanisms that govern secondary phase formation by establishing the influence of processing conditions on phase formation. To accomplish this objective, CoCrNi was first synthesized through a well-established route involving arc melting. The arc-melted material was then subjected to high-pressure torsion (HPT) to promote the formation of a high density of defects, such as grain boundaries and dislocations. A combination of microstructural characterization, high-throughput calculation of phase diagrams (CALPHAD), and hybrid MC/MD simulations is then utilized in an effort to provide fundamental insight into the mechanisms that govern phase decomposition and establish the thermodynamic driving force that drives the formation of one specific secondary phase over the other possible phases.

2. Materials and methods

2.1. Materials synthesis and thermo-mechanical treatments

The CoCrNi alloy was fabricated via arc melting of high-purity elemental metals in Arcast ARC 200. The feedstocks were slugs, wires, and foil with a 99.95 %+ purity by metal basis. During arc melting, a vacuum of 1×10^{-5} torr was pulled on the chamber, and it was then backfilled with commercial purity Ar. The arc-melted buttons were flipped and remelted five times without breaking the inert atmosphere to ensure chemical homogeneity. After the last flip, the liquid metal was tilt-poured into a square mold with a 15 mm × 15 mm cross-section. The final casting was machined into multiple pieces, each with a 6 mm thickness. The material was then homogenized at 1100 °C for 15 h. All the heat treatments were done by encapsulating samples in quartz ampules under a vacuum to prevent material oxidation. The homogenized material was then cold rolled with an 85 % reduction in thickness. The cold-rolled sheets were then sectioned into discs with a diameter of 15 mm using an electrical discharge machine. These discs were subsequently annealed at 900 °C for 1 h to achieve a recrystallized microstructure. This step will be referred to as 'before HPT' in the rest of the paper. The discs were subjected to high-pressure torsion (HPT) at 6.5 GPa, 0.5 rpm, and three rotations. This step will be referred to as 'as-HPT'. The goal of the HPT step was to introduce nanometric grains as well as other defects and potential nucleation sites to decrease the energy required for secondary phase formation.

The HPT disc was then annealed at an intermediate temperature for 350 h to promote the formation of an equilibrium microstructure and induce any possible phase decomposition in this alloy. This step will be referred to as 'long-term annealing.' ThermoCalc, a CALPHAD-based software, was used to determine the temperature for the long-term annealing experiment. Based on the phase stability diagram (Fig. 1a), the temperature selected was 450 °C. Table 2 also shows the predicted composition of different phases at different temperatures. 450 °C is an optimum temperature where 21 vol% of secondary phase formation is expected.

2.2. Oxygen analysis

To determine the amount of oxygen in the material prior to and following HPT and after the long-term annealing treatment, inert gas fusion analysis was performed with the help of an ELTRA Elementrac ONH-p2 analyzer. Three samples were used for each condition, weighing about 130-140 mg. The samples were prepared by polishing on 600 grit SiC paper. A high-purity nickel basket with low oxygen content was also used as a flux for each test to ensure the complete release of the embedded gases. Additional high-purity helium is used as a carrier gas, which helps measure nitrogen in the thermal conductivity cell.

2.3. Microstructural characterization

X-ray diffraction (XRD) was performed using a Rigaku Ultima X-ray diffractometer with a Cu Kα ($\lambda = 0.1542$ nm) radiation source. Electron backscatter diffraction (EBSD) was conducted using a TESCAN GAIA3 dual-beam scanning electron microscope to measure the grain size of the long-term annealed material. The step size used to acquire the EBSD maps was 0.25 μm. The samples for EBSD were hot mounted and polished to 0.05 μm colloidal silica. Scanning/transmission electron microscopy (S/TEM) was used to characterize fine-scale secondary phases and microstructural features using a JEOL JEM-2800 S/TEM operated at 200 kV. To identify crystallographic phases, precession electron diffraction (PED)-based orientation microscopy was performed using ASTAR TM (NanoMEGAS, Brussels, Belgium) hardware and software packages installed on the JEOL JEM-2800 STEM with a 0.5° precession angle and a 1 nm step size.

The secondary phases' atomic structures and elemental distribution were characterized using a JEOL JEM-ARM300F Grand ARM TEM with double Cs correctors operated at 300 kV. A probe current of 35 pA and inner and outer collection angles of 106 and 180 mrad were used for high-angle annular dark field (HAADF) imaging. Energy dispersive X-ray spectroscopy (EDS) chemical maps were acquired with a dual detector system inserted in the large-gap objective pole piece. Samples for TEM analysis were prepared by manually grinding to ~100 μm thickness

Table 2
ThermoCalc predicted composition of various phases at different temperatures under equilibrium conditions using the high entropy alloy database TCHEA6.

Temperature (°C)	*Volume fraction of each phase*		σ phase composition (at%)			FCC matrix composition (at%)		
	Sigma	*FCC*	*Cr*	*Co*	*Ni*	*Cr*	*Co*	*Ni*
450	0.216	0.784	0.609	0.348	0.043	0.257	0.329	0.413
500	0.181	0.819	0.606	0.342	0.052	0.273	0.331	0.395
600	0.097	0.903	0.602	0.329	0.069	0.305	0.333	0.362
691	0.003	0.997	0.599	0.318	0.083	0.333	0.333	0.334
750	0	1.000	0	0	0	0.334	0.333	0.333
900	0	1.000	0	0	0	0.334	0.333	0.333

with a final finish on 1200 SiC grit. 3 mm diameter discs were punched out between the center and the edge. These discs were thinned using twin-jet electropolishing with 10 % perchloric acid in a methanol solution under -25 ºC.

In the four-dimensional (4D)-STEM experiment, the entire convergent beam electron diffraction (CBED) patterns were collected as 2D images for each scan position. In conjunction with the 2D scanning grid, this process generates a 4D dataset. The 4D data were acquired on a JEOL JEM-ARM300F double-aberration-corrected TEM operating at 300 kV. The CBED patterns were captured using a Gatan OneView camera at a frame rate of 300 frames per second (fps), each comprising 1024 × 1024 pixels. We employed a convergence semi-angle of 1 mrad using a 10 μm condenser (C4) and a camera length of 40 cm for the 4D-STEM measurements. The electron probe was raster-scanned across the selected area using a step size of 1.5 nm, and the dwell time is 0.01 s for each step to minimize drift during pattern acquisition.

2.4. High-throughput CALPHAD calculations

The Gibbs energies of the HCP, BCC, and Sigma phases in the CrCoNi system were computed using the high-throughput CALPHAD (HT-CALPHAD) approach at 298 K, 623 K, and 723 K to evaluate the stability of these phases across different temperatures. Compositional variations were generated uniformly across the CrCoNi ternary system with a step size of 2 wt%. For each composition, the Gibbs energy of each phase was calculated at the specified temperatures. Thermo-Calc is used to perform calculations, and the TCHEA6 thermodynamic database was employed. TC-Python, a software package based on Thermo-Calc, is used to perform the high-throughput calculations. About 4,000 calculations are performed for each phase at each of the selected temperatures. Only the phases of interest were included to focus the analysis, while coexisting phases not considered in this study were excluded from the calculations by setting them to dormant. The calculated Gibbs energies were referenced to the stable phases of pure Cr, Co, and Ni elements.

2.5. Monte-Carlo/molecular dynamics simulations

To investigate the possible reason resulting in the formation of a secondary phase, an FCC single crystal model was constructed with the orientation of $[1\bar{1}0]$, $[11\bar{2}]$, and [111] along the x, y, and z directions, respectively. The model comprised 50 × 35 × 20 unit cells and contained 210 000 atoms. There were 60 layers along [111] directions, and an intrinsic stacking fault was first created by shifting the top 45 layers along the $[11\bar{2}]$ direction by the Burgers vector a/6 $[11\bar{2}]$, where a is the lattice constant. Then, the HCP structure with 30 thick lattice layers was created by shifting the neighboring layers along the $[11\bar{2}]$ direction. A modified embedded atom method (MEAM) potential was employed to describe the interatomic interactions of CrCoNi [37]. We use a hybrid Monte Carlo/Molecular Dynamics (MC/MD) simulation method to model local chemical order in the CrCoNi. The MC/MD simulation is performed at 723 K with a Nose-Hoover thermostat. 10,000 MD steps were carried out, and MC trails were performed every 100 MD steps to enable 2000 atom swaps for each pair of elements.

3. Results

3.1. Inert gas fusion analysis

Table 3 lists the oxygen and nitrogen content in the material before HPT, as-HPT, and long-term annealed state. A small amount of oxygen, around 139 ppm, was present in the material before it underwent HPT. Even though high-purity feedstock was used during arc melting and the heat treatments were done under vacuum encapsulation, oxygen cannot be entirely avoided during processing. The oxygen level increases slightly during the HPT processing and long-term annealing, but only by ~13 ppm. It should be noted that, as stated earlier, the heat treatment was done under vacuum encapsulation to prevent oxidation of samples. That is why there is no significant increase in the oxygen content of the material, even after 350 h of annealing. Nitrogen shows a similar trend as well where there is only a small increase in its content before HPT (~74 ppm) as compared to the long-term annealed state (~82 ppm).

3.2. Microstructural characterization

XRD was performed to analyze the phase formation in the material further. Fig. 1b represents the XRD pattern of the alloy after different processing steps. The peaks observed in the before HPT, as-HPT, and long-term annealed alloys verify the presence of the FCC phase in all conditions. The alloy's peaks before HPT indicate a single FCC phase. Similar peaks were observed in the as-HPT alloy. However, the peaks at 2θ values of 51.2° and 75.4° have broadened significantly, indicating the formation of nanometric grains. No distinct peaks related to the secondary phase were observed in the as-HPT condition. In the case of the long-term annealed alloy, two faint peaks at 2θ values of ~47.2° and ~62.2° were observed in addition to the distinct FCC phase peaks. Fig. 1c shows a zoomed-in view of the pattern from 2θ values of 46° and 64°. The diamond sign highlights the additional peaks. Analysis using the Rigaku PDXL 2 software indicates that these peaks are similar to those observed in the Co HCP phase or a Co-Cr alloy. By calculating the d spacing based on the given peak positions, these peaks are expected to correspond to (101) and (102) planes of the Co-rich HCP phase. However, in-depth analysis, apart from XRD, is needed to accurately determine the phase these additional peaks originate from.

Further microstructural characterization of the alloys in as-HPT and long-term annealed state was done using TEM. Fig. 2a depicts the microstructure of the CoCrNi in the as-HPT condition. Ultrafine grains with dense deformation structures were observed. Such microstructural features are typical for alloys undergoing severe plastic deformation. As shown by Zhilyaev et al. [38], the microstructure after HPT is

Table 3
Elemental analysis of oxygen and nitrogen in the alloy after different processing steps.

Alloy condition	O [ppm]	N [ppm]
Before HPT	139 ± 5	74 ± 4
As-HPT	145 ± 3	79 ± 2
Long-term annealed	152 ± 3	82 ± 1

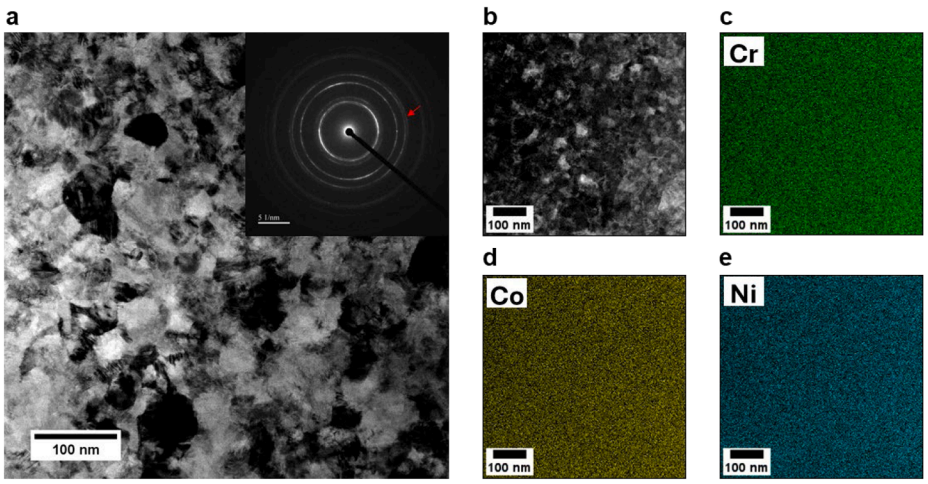

Fig. 2. (a) TEM bright-field image of as-HPT alloy .The inset represents the selected area electron diffraction pattern of as-HPT alloy (b-e) Another TEM bright field image from the as-HPT alloy and corresponding STEM-EDS highlighting the elemental distribution of Co, Cr, Ni respectively.

characterized by nanometric grains with poorly defined grain boundaries, which suggests high levels of internal stresses. Such processes generally lead to an increase in the density of dislocations, twins, and other defects as observed in various studies [39–45]. The inset in Fig. 2a represents the electron diffraction pattern of the alloy in an as-HPT state. The rings in the diffraction pattern point to the presence of nanocrystalline grains with random crystal orientations. The pattern also indicates the presence of an FCC phase with a lattice parameter of ~3.63 Å, which is close to the reported values of the CoCrNi lattice parameter [46,47]. The electron diffraction pattern also shows a faint ring (indicated by red arrow) which might correspond to another phase but it's challenging to confirm it microstructurally given the high amount of deformation. Fig. 2b-e represents the STEM-EDS of the as-HPT alloy, which shows a uniform distribution of Co, Cr, and Ni, and no elemental segregation was observed.

The alloy's microstructure after long-term annealing at 450 °C was analyzed using SEM-EBSD. Fig. 3a represents the grain structure of the long-term annealed alloy, and it can be clearly seen that the grain size increased from an average of ~45 nm in the as-HPT alloy to micron-sized grains in the long-term annealed alloy. The microstructure of the long-term annealed alloy is characterized by elongated grains, with an average grain diameter of 2.74 μm. Fig. 3b represents a TEM micrograph of the long-term annealed alloy, which also confirms the grain growth after annealing as compared to the as-HPT state (in Fig. 2a)

TEM of the long-term annealed alloy also highlighted the presence of precipitates or inclusions at some grain boundaries and triple junctions in this alloy. Because of their small size, they could not be well resolved in SEM-EBSD but were observed during TEM, as shown in Fig. 4a. Fig. 4 (b-e) and 4f represent the STEM-EDS maps and electron diffraction pattern corresponding to the micrograph in Fig. 4a, respectively. In this case, it confirms the presence of Cr-rich oxide (with approximately 70.5 at% Cr, 19 at% O, 5.5 at% Co, and 5 at% Ni) at the grain boundaries of the long-term annealed CoCrNi alloy.

Another interesting feature detected in the microstructure of the long-term annealed CoCrNi alloy is the presence of rod-like precipitates, as shown in Fig. 5a. It was observed that such precipitates had one end at the grain boundary and extended inside the grain interior, sometimes also spreading across an entire grain. STEM-EDS was conducted to identify this precipitate's chemical composition, shown in Fig. 5b-g. The rod-like precipitates were found to be rich in cobalt (~40.5 at% Co) and chromium (~35.5 at% Cr) and slightly depleted in nickel (~24 at% Ni). It was also confirmed that these precipitates had no enrichment of oxygen, carbon, or nitrogen. Please note this precipitate was found near a Cr-rich oxide, but the STEM-EDS maps in Fig. 5b-g only focus on the composition of the precipitate and not the nearby oxide. The observed precipitates' chemical composition differed from the Cr-rich sigma phase that was predicted to form after long-term annealing at 450 °C, as mentioned earlier in Table 2 and Fig. 1a.

Atomic-resolution HAADF-STEM was conducted to elucidate the phase structure of the precipitate further. Fig. 6a represents a high-magnification view of the precipitation within the FCC matrix. Fig. 6b shows that the atoms in the precipitate region have ABABABAB... stacking sequence, indicating an HCP structure. The FCC/HCP interface is parallel to the (111) plane of the FCC matrix, aligning with the

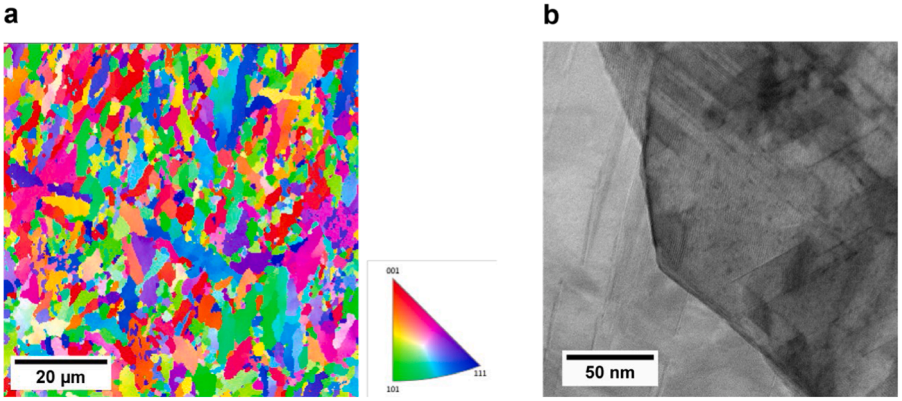

Fig. 3. (a) SEM-EBSD represents the grain structure after long-term annealing (b) TEM dark-field image of the long-term annealed CoCrNi alloy.

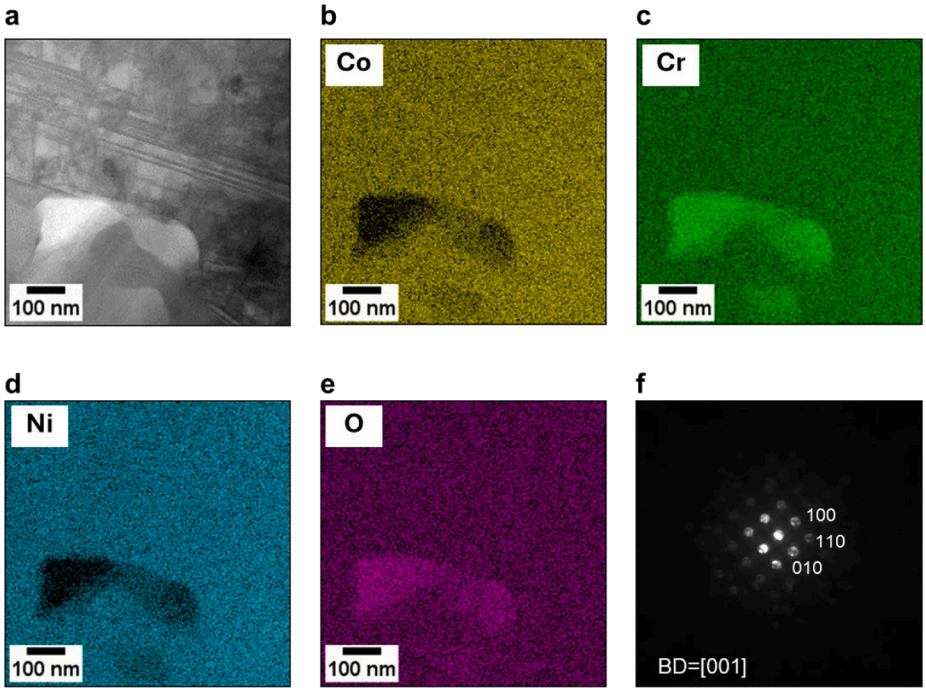

Fig. 4. (a) TEM dark-field image of an oxide observed at the grain boundary and (b-e) corresponding STEM-EDS highlighting the elemental distribution of Co, Cr, Ni, and O in the observed oxide (f) electron diffraction pattern of the Cr-rich oxide.

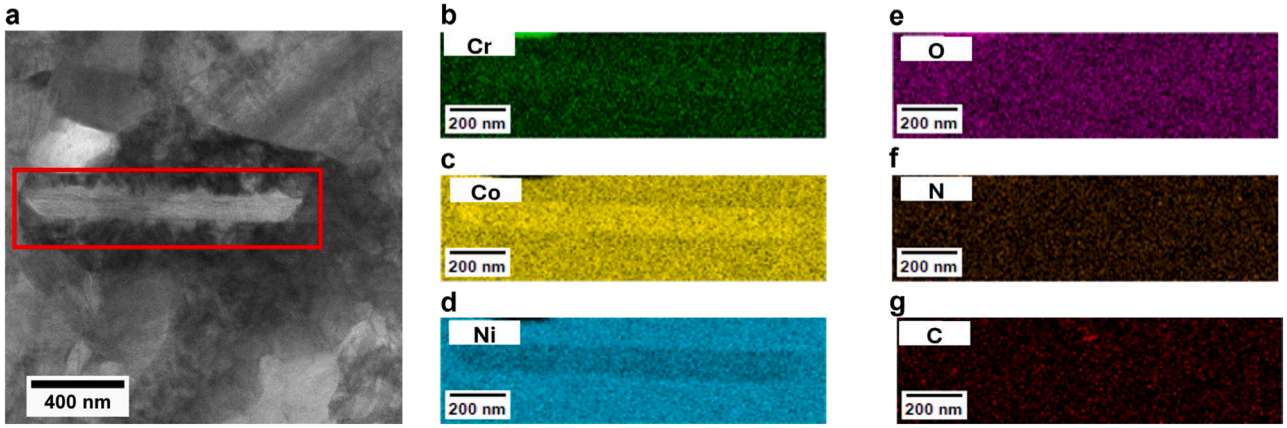

Fig. 5. (a) TEM bright field image highlighting the precipitate observed after long-term annealing (b-g) STEM-EDS of the rod-like precipitate in a red box (4a) showing elemental distribution of Cr, Co, Ni, O, N, and C respectively.

stacking faults, which indicates that this HCP phase nucleated at a stacking fault. Since it can be difficult for readers to discern the atomic sequence clearly, Fig. 6c shows a Fast Fourier Transform (FFT) pattern confirming the precipitate's HCP crystal structure. Moreover, Fig. 6d represents a virtual dark field image of HCP and FCC phases, and the red circle indicates the virtual aperture as shown in the diffraction pattern. The corresponding electron diffraction patterns extracted from the 4D-STEM data further establish the presence of HCP precipitate in the long-term annealed alloy

To distinguish the structure of the precipitates from that of a twin or a stacking fault (which are also local regions of HCP stacking in an FCC matrix), precession electron diffraction (PED) analysis was conducted. The results of the PED analysis are shown in Fig. 7 below. Fig. 7b and 7c illustrate orientation and phase maps for the microstructure depicted in 7a. The rod-like precipitate spanning the grain was confirmed to be a secondary phase with an HCP crystal structure. Combining all the TEM analysis from Figs. 5–7, it can be confirmed that long-term annealing at an intermediate temperature promoted the formation of a secondary phase with an HCP structure in the HPT-processed CoCrNi alloy.

3.3. Calculation of Gibbs energy of phase formation

The Gibbs energies of various phases were calculated using HT-CALPHAD to explore the driving forces behind the secondary phase formation. Fig. 8a represents the isothermal section of the Co-Cr-Ni system at 450 °C, highlighting the formation of four major phases: Sigma, HCP, BCC, and FCC. Fig. 8b, c, and d illustrate the Gibbs energy differences of Sigma, BCC, and HCP phases with FCC as the reference state during annealing at 450 °C under equilibrium conditions, with the blue dot at the center representing the $Co_1Cr_1Ni_1$ equiatomic composition. The calculations reveal that FCC at the equiatomic composition exhibits the lowest Gibbs energy. The Sigma, HCP, and BCC phases show slightly higher Gibbs energies, with HCP slightly lower than Sigma and BCC. However, the phase diagram in Fig. 8a indicates that the

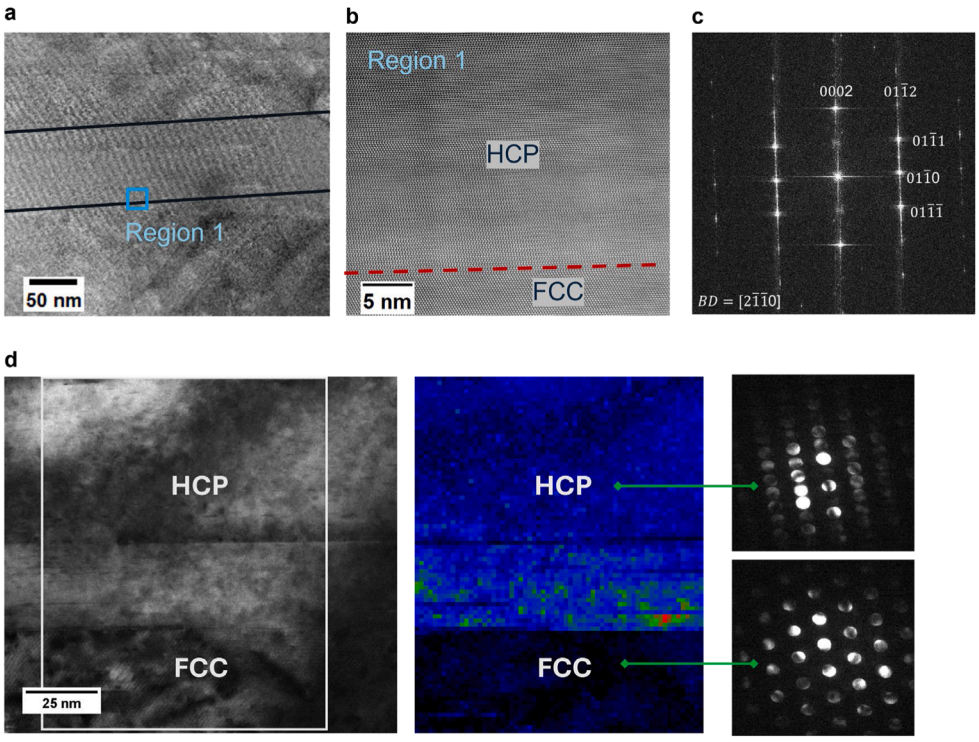

Fig. 6. (a) and (b) Atomic resolution HAADF STEM images of the secondary phase formed in the FCC, showing an HCP atomic arrangement (c) FFT pattern corresponding to the HCP precipitate shown in b, (d) 4D-STEM micrographs and virtually generated dark field images and corresponding electron diffraction patterns.

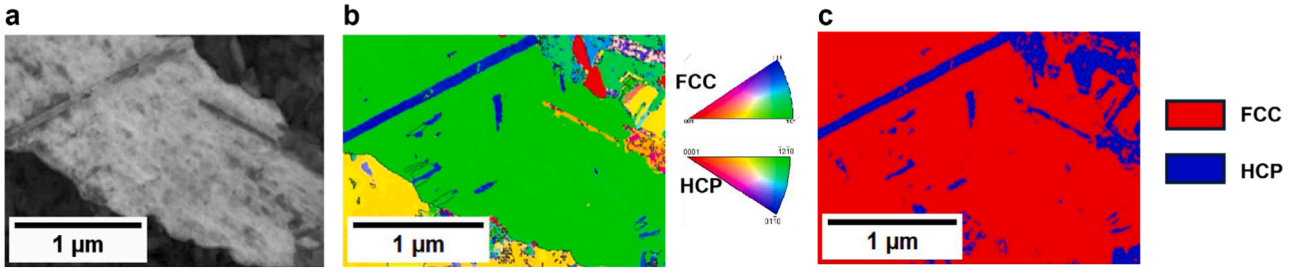

Fig. 7. Precession electron diffraction (PED) analysis on the CrCoNi alloy. (a) PED bright-field images. (b) PED inverse pole figure (IPF) maps, highlighting crystallographic orientation. (c) PED phase map, showing a hcp precipitate extending across the grain.

equiatomic composition resides within the two-phase region of FCC and Sigma at 450 °C. The detailed analysis of the Gibbs energy and phase stability will be covered in Section 4.1.

3.4. Monte-Carlo/molecular dynamics simulations

A hybrid MC/MD simulation method was performed on a model with an HCP lamella in the middle of the FCC matrix, as shown in Fig. 9a. The initial atomic ratios of Co, Cr, and Ni were fixed at 35 %, 31 % and 34 % respectively (Cr-depleted matrix), based on the STEM-EDS results from the matrix region of as annealed alloy (~ 33 %, 31 %, and 32 %, respectively). Initially, three elements were randomly distributed, and MC/MD simulation was performed at 723 K(450 °C) for 10,000 MD steps. After MC/MD simulation, the distribution of atoms is shown in Fig. 9b. There appears to be more Cr in the HCP lamella, while Ni segregates in the FCC matrix. To quantify how each element varies on the FCC matrix and HCP lamella, we compute the atomic percentage of elements on every lattice layer along [111] direction, as shown in Fig. 9c. In the FCC matrix, the atomic ratios of Co, Cr, and Ni are about 35 %, 29 %, and 36 %, respectively. In contrast, in HCP lame, the atomic ratios are about 35 %, 33 %, and 32 %, respectively. The results show Ni depletion and Cr aggregation in HCP lamella, and Co seems to have no preference in the two phases. These results will be further discussed in Section 4.2.

4. Discussion

4.1. Formation of HCP phase over sigma phase

As mentioned in Section 2.1, a Cr-rich sigma phase was expected to be formed from the $Co_1Cr_1Ni_1$ equiatomic composition at 450 °C, as shown in Fig. 8a. Such Cr-rich sigma phase formation has also been observed in similar FCC CCAs such as CoCrFeMnNi [9,10] and CoCrFeNi [19]. Hence, it is intriguing that such sigma phase formation had not been reported for the equiatomic $Co_1Cr_1Ni_1$ despite this alloy's relatively higher content of Cr.

As shown in Fig. 1a, the Sigma phase is predicted to be in equilibrium at temperatures below 700 °C. The current work calculates the molar Gibbs energy for the liquid, Sigma, HCP, and FCC phases at 450 °C along the Co_1Cr_1-Ni composition section, as shown in Fig. 10. At this temperature, only a very small amount of the Sigma phase is observed to be in equilibrium with the FCC matrix. Even though the composition section is not along the FCC-sigma phase tie-line, it is good enough to

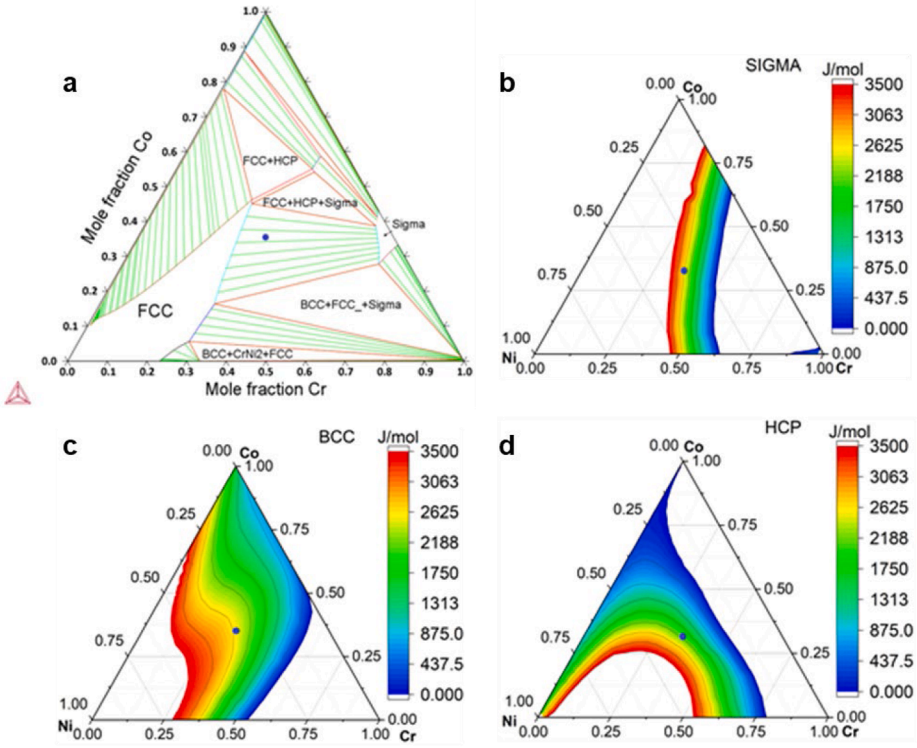

Fig. 8. (a) Co-Cr-Ni isothermal section at 450 °C, blue dot represents the equiatomic composition (b-d) Gibbs energy differences of sigma, BCC, and HCP phases with FCC at 450 °C.

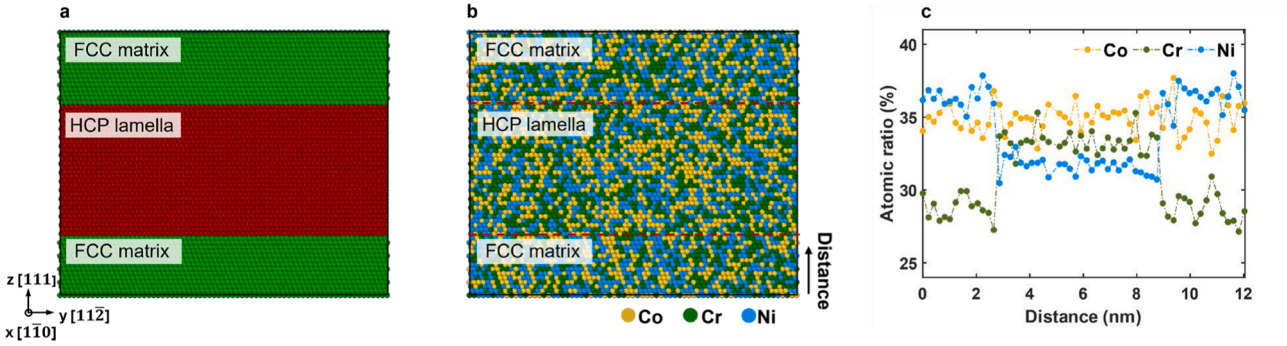

Fig. 9. The chemical distribution after MC/MD simulation. (a) The structure of the simulation model. (b) The distribution of atoms after MC/MD simulation on an atomic slide. (c) The atomic ratio of elements along [111] direction.

capture the thermodynamics involved.

The results indicate that FCC exhibits the lowest molar Gibbs energy at the equiatomic $Co_1Cr_1Ni_1$ composition (the blue solid line), followed by HCP, the Sigma phase, and liquid. Assuming the tie line exists in this composition section, it shows the equiatomic $Co_1Cr_1Ni_1$ FCC will enter the FCC and sigma two-phase region, based on the standard tangent line (the blue dash line), i.e., a small amount of sigma phase will precipitate out of the FCC matrix, which is in good agreement with the simulation from Fig. 1a. It is worth noting that the formed sigma phase will be far from the equiatomic $Co_1Cr_1Ni_1$ composition. Meanwhile, simply comparing the Gibbs energy of all these four phases at the equiatomic $Co_1Cr_1Ni_1$ composition, the HCP phase has a higher driving force to directly form from FCC without composition change than the Sigma phase, which is consistent with experimental observations of HCP formation from the FCC matrix in this work. Furthermore, the equiatomic CoCrNi is a low stacking fault energy (~ 22 mJ/m^2 [48]) alloy, which means the formation of stacking faults is favored in this alloy. Typically, stacking faults are regions of HCP stacking (not a different phase) in an FCC matrix. When multiple stacking faults overlap with each other, it can also aid the formation of the HCP phase [49,50] . The detailed mechanism of how stacking faults help in HCP phase formation will be discussed in the next section.

4.2. *Mechanism of HCP phase formation in severely deformed CoCrNi*

The HCP phase formation observed in this work can be similar to the strain-induced epsilon martensitic formation observed in steels and other conventional alloys [50–54]. For such transformations, specific stacking faults further lead to the nucleation of the HCP martensite phase with no compositional change during the transformation [50]. The mechanism of how a stacking fault can trigger the nucleation of an HCP phase is discussed in detail by He et al. [49]. It should be noted that they reported the FCC to HCP phase formation in a 'bulk' sample at 15K under tensile loading and attributed the formation of the HCP phase to the gliding of the Shockley partials on every other plane. Fujita and Yuda [50] also highlighted the mechanism for FCC to HCP transformation in

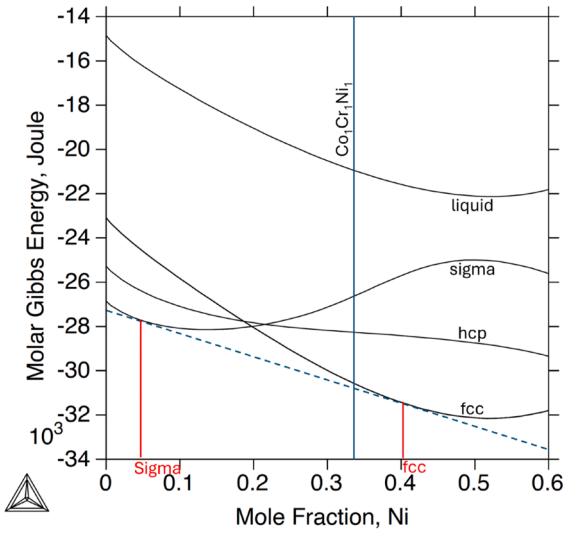

Fig. 10. The molar Gibbs energy diagram of the Co_1Cr_1-Ni composition section at 450 °C, crossing the equiatomic $Co_1Cr_1Ni_1$ composition in the Co-Cr-Ni ternary system.

18-8 type stainless steel. In their work, they concluded that the stacking faults firstly form on {111} slip planes. This further induced the formation of more stacking faults on the same plane as it minimized the bulk free energy and the stacking fault energy. This way, the stacking faults form on every other plane, and when they overlap, the HCP phase is formed. Similar mechanisms can be applied to the CoCrNi alloy in this study, which has undergone severe deformation through HPT. Such processes introduce a high density of stacking faults in the alloy, which can act as an embryo for the HCP phase formation. In this work, it was confirmed through the HAADF STEM images in Fig. 6b and the corresponding FFT image in Fig. 6c that the HCP's basal plane is coplanar with the FCC (111) plane. This indicates that a strain-induced HCP nano-lamella formed during HPT.

Furthermore, the formation of compositionally distinct HCP phase in this work is similar to that of Manganese partitioning in TRIP/TWIP steels [55,56]. Along the same line in CoCrNi, there are abundant HCP lamellae present in as-HPT material. The presence of Cr-rich oxides results in a Ni and Co-rich matrix. Therefore, during annealing at 450 °C, Co, being an HCP stabilizer, moves into the region of HCP lamella, resulting in a compositionally partitioned HCP phase. To highlight the influence of long-term annealing on the chemical composition of the HCP phase, hybrid MC/MD simulations were utilized, as shown in Fig. 9. This simulation created an HCP lamella, representing the precipitate, within an FCC matrix. The system was annealed at 450 °C to see the preferential arrangement of elements in the precipitate and matrix. The simulation shows that Cr prefers to be in the precipitate while Ni does not. Co is evenly distributed between the precipitate and matrix. However, in the experimental data, Co also shows enrichment in HCP lamella. The difference might arise due to the lack of oxygen in our model, given the limitation of the potential used. Without considering Cr-oxides in our model, however, the depletion of Ni and aggregation of Cr in HCP lamella still imply that the long-term annealing favors the precipitate to attain the elemental distribution that is energetically favorable. Additionally, the tendency of Co to favor HCP phase in other alloys has also been highlighted in the different experimental studies by Wang et al. [57] and Zhang et al. [58].

4.3. Correlating phase decomposition with processing artifacts

While the FCC to HCP phase transformation has been previously reported [33–36] in the equiatomic $Co_1Cr_1Ni_1$, the reason why the HCP phase forms, not the sigma phase, has not been discussed in detail. This work attempts to answer that question. There are two main factors behind this observation. First, this alloy's low SFE will help compensate for the energy difference between FCC and HCP and stabilize HCP, as shown in Fig. 10. The second factor is the local composition variation. Fig. 11a shows Cr-rich oxides (red circles) near precipitates (yellow dotted box). Fig. 11b and c represent the STEM-EDS of the precipitates and one of the oxides, respectively, to confirm their composition. It is observed that these precipitates generally form in the vicinity of the Cr-rich oxides.

Microstructurally, the formation of Cr-rich oxides will cause a local fluctuation in the composition of the matrix around it, making it slightly deficient in Cr. Hence, the matrix around the oxide will deviate from an equiatomic composition and move towards a Cr-depleted composition, as indicated by the black arrows in Fig. 11d and e. Such a change in local composition does not affect the Gibbs energy of HCP phase formation (Fig. 11d), but it leads to an even higher Gibbs energy of sigma phase formation, as shown in Fig. 11e. This will further promote the formation of the HCP phase over the sigma phase. Hence, a low SFE of the equiatomic CoCrNi alloy combined with the severe deformation during HPT and processing artifacts like the formation of Cr-rich oxide makes it easier for the HCP phase to precipitate under such conditions in this study. The combined effect of these factors leading to precipitation of HCP phase is illustrated in the schematic shown in Fig. 11f.

5. Conclusions

This work investigates phase decomposition in a high-pressure torsioned CoCrNi alloy that was annealed for a prolonged time at 450 °C for 350 h. XRD, S/TEM, and PED were utilized to microstructurally characterize the secondary phase, which formed from the decomposition of the significant FCC matrix phase. High-throughput CALPHAD and MC/MD simulations were used to elucidate the mechanisms driving the secondary phase formation in this equiatomic CoCrNi alloy. The main conclusions from this study are:

a) A secondary phase precipitated during prolonged annealing at 450 °C. It was rich in Co and Cr and depleted in Ni. This phase's HCP structure was confirmed, which differed from previous predictions and observations of the sigma phase formation.
b) Based on initial thermodynamic equilibrium calculations, the sigma phase was initially expected to precipitate from the FCC matrix. High-throughput CALPHAD showed the formation of an HCP phase to be more energetically favorable than the sigma phase. The lowest Gibbs energy difference exists between the HCP and FCC phases at the equiatomic $Co_1Cr_1Ni_1$ composition, leading to the HCP phase precipitating out of the FCC matrix with minimal local compositional change.
c) The high density of stacking faults due to HPT and the low SFE of the CoCrNi alloy can act as nucleation sites for the HCP phase and significantly promote its formation. The long-term annealing further provides the driving force for elemental rearrangement within the HCP phase formed during HPT.
d) The presence of impurities like Cr-rich oxide also impacts the phase formation in the CoCrNi alloy. The formation of such oxide leads to local fluctuations in the composition, which further supports the formation of the HCP phase over sigma. Hence, such potential impurities must be considered when considering the phase stability of complex concentrated alloys.

CRediT authorship contribution statement

Sakshi Bajpai: Writing – original draft, Visualization, Validation, Investigation, Formal analysis, Data curation. **Xin Wang:** Visualization, Validation, Investigation. **Bijun Xie:** Writing – review & editing, Visualization, Validation, Investigation. **Hangman Chen:** Validation, Investigation. **Jize Zhang:** Visualization, Formal analysis. **Calvin**

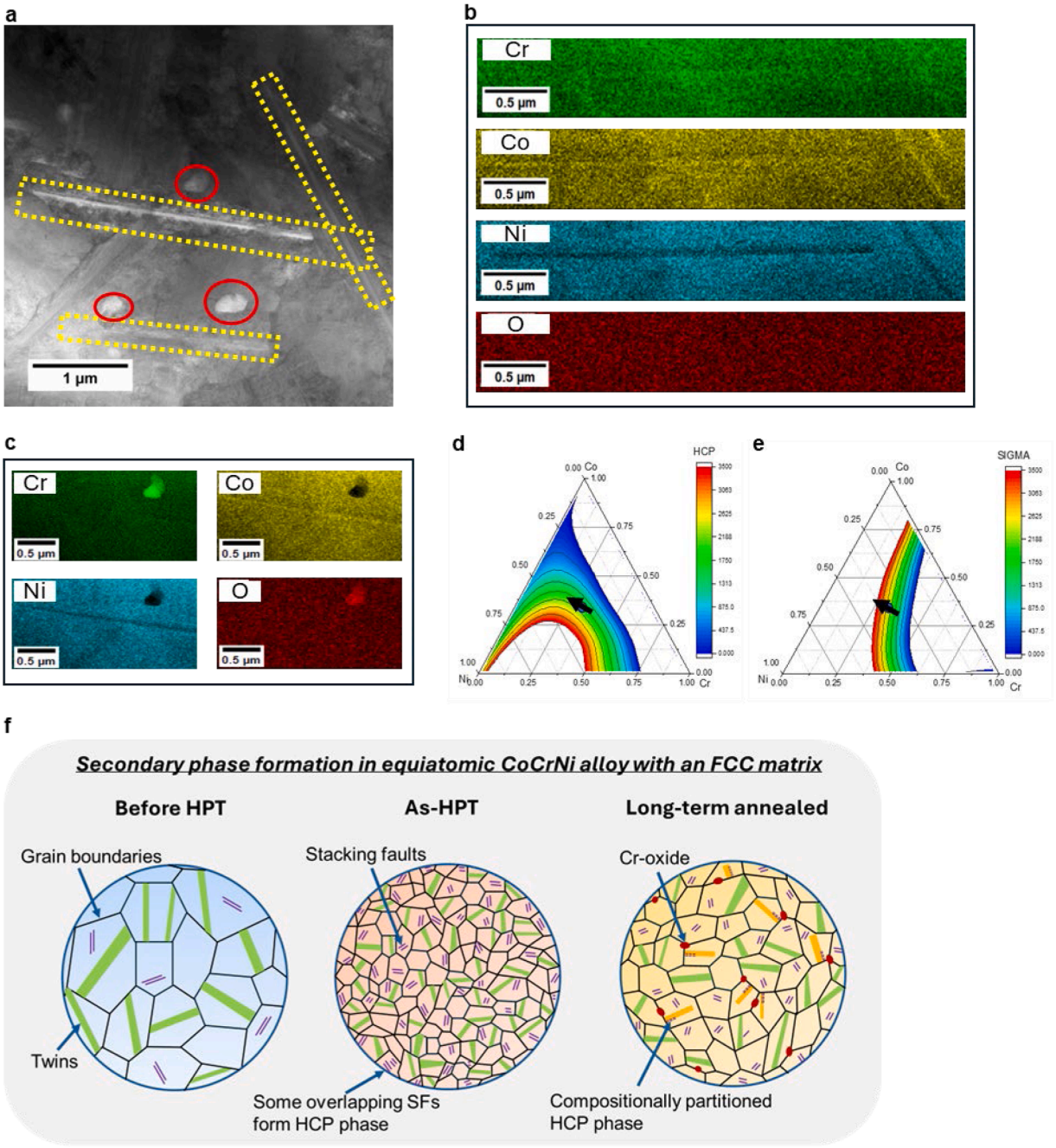

Fig. 11. TEM micrograph of the alloy after long-term annealing. The precipitates are shown in yellow rectangular boxes. The Cr-rich oxides are circled in red (b) STEM-EDS of HCP precipitates in yellow boxes (c) STEM-EDS of one of the oxides in red circle (d) and (e) Gibbs energy map for HCP and sigma phase formation with a FCC matrix of equiatomic CoCrNi at 450 °C (f) Schematic explaining HCP phase formation in this study.

Belcher: Writing – review & editing, Formal analysis. **Benjamin MacDonald:** Writing – review & editing, Methodology, Conceptualization. **Julia Ivanisenko:** Writing – review & editing, Resources, Investigation. **Yu Zhong:** Writing – original draft, Visualization, Validation, Formal analysis. **Penghui Cao:** Writing – review & editing, Supervision, Conceptualization. **Enrique J. Lavernia:** Writing – review & editing, Supervision, Funding acquisition. **Diran Apelian:** Writing – review & editing, Supervision, Funding acquisition.

Declaration of competing interest

The authors declare they have no known competing financial interests or personal relationships that could have influenced this paper.

Acknowledgments

This research was primarily supported by the National Science Foundation Materials Research Science and Engineering Center program through the UC Irvine Center for Complex and Active Materials (DMR-2011967). The authors also acknowledge the use of facilities and instrumentation at the UC Irvine Materials Research Institute (IMRI), supported in part by the National Science Foundation Materials Research Science and Engineering Center program through the UC Irvine Center for Complex and Active Materials (DMR-2011967). E.J. Lavernia acknowledges support provided by the State of Texas Governor's University Research Initiative (GURI) and the Texas A&M University Chancellor's Research Initiative (CRI).

References

[1] D.B. Miracle, O.N. Senkov, A critical review of high entropy alloys and related concepts, Acta Mater. 122 (2017) 448–511, https://doi.org/10.1016/j.actamat.2016.08.081.

[2] S. Gorsse, D.B. Miracle, O.N. Senkov, Mapping the world of complex concentrated alloys, Acta Mater. 135 (2017) 177–187, https://doi.org/10.1016/j.actamat.2017.06.027.

[3] E.P. George, D. Raabe, R.O. Ritchie, High-entropy alloys, Nat. Rev. Mater. 4 (2019) 515–534, https://doi.org/10.1038/s41578-019-0121-4.

[4] D.B. Miracle, High entropy alloys as a bold step forward in alloy development, Nat. Commun. 10 (2019) 1805, https://doi.org/10.1038/s41467-019-09700-1.

[5] E.P. George, W.A. Curtin, C.C. Tasan, High entropy alloys: a focused review of mechanical properties and deformation mechanisms, Acta Mater. 188 (2020) 435–474, https://doi.org/10.1016/j.actamat.2019.12.015.

[6] B. Cantor, Multicomponent high-entropy cantor alloys, Prog. Mater. Sci. 120 (2021) 100754, https://doi.org/10.1016/j.pmatsci.2020.100754.

[7] B. Gludovatz, A. Hohenwarter, D. Catoor, E.H. Chang, E.P. George, R.O. Ritchie, A fracture-resistant high-entropy alloy for cryogenic applications, Science 345 (2014) 1153–1158, https://doi.org/10.1126/science.1254581.

[8] F. Otto, A. Dlouhý, Ch. Somsen, H. Bei, G. Eggeler, E.P. George, The influences of temperature and microstructure on the tensile properties of a CoCrFeMnNi high-entropy alloy, Acta Mater. 61 (2013) 5743–5755, https://doi.org/10.1016/j.actamat.2013.06.018.

[9] F. Otto, A. Dlouhý, K.G. Pradeep, M. Kuběnová, D. Raabe, G. Eggeler, E.P. George, Decomposition of the single-phase high-entropy alloy CrMnFeCoNi after prolonged anneals at intermediate temperatures, Acta Mater. 112 (2016) 40–52, https://doi.org/10.1016/j.actamat.2016.04.005.

[10] N. Park, B.-J. Lee, N. Tsuji, The phase stability of equiatomic CoCrFeMnNi high-entropy alloy: comparison between experiment and calculation results, J. Alloys Compd. 719 (2017) 189–193, https://doi.org/10.1016/j.jallcom.2017.05.175.

[11] B.E. MacDonald, Z. Fu, X. Wang, Z. Li, W. Chen, Y. Zhou, D. Raabe, J. Schoenung, H. Hahn, E.J. Lavernia, Influence of phase decomposition on mechanical behavior of an equiatomic CoCuFeMnNi high entropy alloy, Acta Mater. 181 (2019) 25–35, https://doi.org/10.1016/j.actamat.2019.09.030.

[12] B. Schuh, F. Mendez-Martin, B. Völker, E.P. George, H. Clemens, R. Pippan, A. Hohenwarter, Mechanical properties, microstructure and thermal stability of a nanocrystalline CoCrFeMnNi high-entropy alloy after severe plastic deformation, Acta Mater. 96 (2015) 258–268, https://doi.org/10.1016/j.actamat.2015.06.025.

[13] G. Qin, R. Chen, H. Mao, Y. Yan, X. Li, S. Schönecker, L. Vitos, X. Li, Experimental and theoretical investigations on the phase stability and mechanical properties of Cr7Mn25Co9Ni23Cu36 high-entropy alloy, Acta Mater. 208 (2021) 116763, https://doi.org/10.1016/j.actamat.2021.116763.

[14] Y. Cao, W. Zhang, B. Liu, Y. Liu, M. Du, A. Fu, Phase decomposition behavior and its effects on mechanical properties of TiNbTa0.5ZrAl0.5 refractory high entropy alloy, J. Mater. Sci. Technol. 66 (2021) 10–20, https://doi.org/10.1016/j.jmst.2020.05.038.

[15] M. Huang, J. Jiang, Y. Wang, Y. Liu, Y. Zhang, Microstructure evolution, phase decomposition and transition of Al0.8Co0.5Cr1.5CuFeNi HEA during high temperature sintering and mechanical properties corresponding to different microstructures, Mater. Des. 223 (2022) 111167, https://doi.org/10.1016/j.matdes.2022.111167.

[16] B. Schuh, B. Völker, J. Todt, N. Schell, L. Perrière, J. Li, J.P. Couzinié, A. Hohenwarter, Thermodynamic instability of a nanocrystalline, single-phase TiZrNbHfTa alloy and its impact on the mechanical properties, Acta Mater. 142 (2018) 201–212, https://doi.org/10.1016/j.actamat.2017.09.035.

[17] C. Ng, S. Guo, J. Luan, S. Shi, C.T. Liu, Entropy-driven phase stability and slow diffusion kinetics in an Al0.5CoCrCuFeNi high entropy alloy, Intermetallics 31 (2012) 165–172, https://doi.org/10.1016/j.intermet.2012.07.001.

[18] B. Ren, Z.X. Liu, B. Cai, M.X. Wang, L. Shi, Aging behavior of a CuCr2Fe2NiMn high-entropy alloy, Mater. Des. 33 (2012) 121–126, https://doi.org/10.1016/j.matdes.2011.07.005.

[19] F. He, Z. Wang, Q. Wu, J. Li, J. Wang, C.T. Liu, Phase separation of metastable CoCrFeNi high entropy alloy at intermediate temperatures, Scr. Mater. 126 (2017) 15–19, https://doi.org/10.1016/j.scriptamat.2016.08.008.

[20] R. Feng, M.C. Gao, C. Zhang, W. Guo, J.D. Poplawsky, F. Zhang, J.A. Hawk, J. C. Neuefeind, Y. Ren, P.K. Liaw, Phase stability and transformation in a light-weight high-entropy alloy, Acta Mater. 146 (2018) 280–293, https://doi.org/10.1016/j.actamat.2017.12.061.

[21] B. Gwalani, S. Gorsse, D. Choudhuri, M. Styles, Y. Zheng, R.S. Mishra, R. Banerjee, Modifying transformation pathways in high entropy alloys or complex concentrated alloys via thermo-mechanical processing, Acta Mater. 153 (2018) 169–185, https://doi.org/10.1016/j.actamat.2018.05.009.

[22] Y.-X. Zhuang, X.-L. Zhang, X.-Y. Gu, Effect of annealing on microstructure and mechanical properties of Al0.5CoCrFeMoxNi high-entropy alloys, Entropy 20 (2018) 812, https://doi.org/10.3390/e20110812.

[23] A.S. Rogachev, S.G. Vadchenko, D.Yu. Kovalev, N.A. Kochetov, M. Zhukovskyi, T. Orlova, A.S. Mukasyan, Long term stability of a high-entropy CoCrFeNiTi alloy fabricated by mechanical alloying, J. Alloys Compd. 931 (2023) 167470, https://doi.org/10.1016/j.jallcom.2022.167470.

[24] A. Karati, K. Guruvidyathri, V.S. Hariharan, B.S. Murty, Thermal stability of AlCoFeMnNi high-entropy alloy, Scr. Mater. 162 (2019) 465–467, https://doi.org/10.1016/j.scriptamat.2018.12.017.

[25] Y.H. Meng, F.H. Duan, J. Pan, Y. Li, Phase stability of B2-ordered ZrTiHfCuNiFe high entropy alloy, Intermetallics 111 (2019) 106515, https://doi.org/10.1016/j.intermet.2019.106515.

[26] S. Mohanty, N.P. Gurao, P. Padaikathan, K. Biswas, Ageing behaviour of equiatomic consolidated Al20Co20Cu20Ni20Zn20 high entropy alloy, Mater. Charact. 129 (2017) 127–134, https://doi.org/10.1016/j.matchar.2017.04.011.

[27] V. Shivam, Y. Shadangi, J. Basu, N.K. Mukhopadhyay, Alloying behavior and thermal stability of mechanically alloyed nano AlCoCrFeNiTi high-entropy alloy, J. Mater. Res. 34 (2019) 787–795, https://doi.org/10.1557/jmr.2019.5.

[28] J.Q. Yao, X.W. Liu, N. Gao, Q.H. Jiang, N. Li, G. Liu, W.B. Zhang, Z.T. Fan, Phase stability of a ductile single-phase BCC Hf0.5Nb0.5Ta0.5Ti1.5Zr refractory high-entropy alloy, Intermetallics 98 (2018) 79–88, https://doi.org/10.1016/j.intermet.2018.04.023.

[29] B. Schuh, B. Völker, V. Maier-Kiener, J. Todt, J. Li, A. Hohenwarter, Phase decomposition of a single-phase AlTiVNb high-entropy alloy after severe plastic deformation and annealing, Adv. Eng. Mater. 19 (2017) 1600674, https://doi.org/10.1002/adem.201600674.

[30] B. Gludovatz, A. Hohenwarter, K.V.S. Thurston, H. Bei, Z. Wu, E.P. George, R. O. Ritchie, Exceptional damage-tolerance of a medium-entropy alloy CrCoNi at cryogenic temperatures, Nat. Commun. 7 (2016) 10602, https://doi.org/10.1038/ncomms10602.

[31] Z. Wu, H. Bei, F. Otto, G.M. Pharr, E.P. George, Recovery, recrystallization, grain growth and phase stability of a family of FCC-structured multi-component equiatomic solid solution alloys, Intermetallics 46 (2014) 131–140, https://doi.org/10.1016/j.intermet.2013.10.024.

[32] Z. Wu, H. Bei, G.M. Pharr, E.P. George, Temperature dependence of the mechanical properties of equiatomic solid solution alloys with face-centered cubic crystal structures, Acta Mater. 81 (2014) 428–441, https://doi.org/10.1016/j.actamat.2014.08.026.

[33] B. Schuh, B. Völker, J. Todt, K.S. Kormout, N. Schell, A. Hohenwarter, Influence of annealing on microstructure and mechanical properties of a nanocrystalline CrCoNi medium-entropy alloy, Materials 11 (2018) 662, https://doi.org/10.3390/ma11050662.

[34] H.W. Deng, K. Jing, W.Y. Du, Z.Y. Liu, Z.M. Xie, T. Zhang, H. Li, B. Liu, The annealing induced formation of epsilon martensite in CoCrNi medium-entropy alloy after severe plastic deformation, J. Alloys Compd. 899 (2022) 163349, https://doi.org/10.1016/j.jallcom.2021.163349.

[35] I. Moravcik, J. Cizek, Z. Kovacova, J. Nejezchlebova, M. Kitzmantel, E. Neubauer, I. Kubena, V. Hornik, I. Dlouhy, Mechanical and microstructural characterization of powder metallurgy CoCrNi medium entropy alloy, Mater. Sci. Eng.: A 701 (2017) 370–380, https://doi.org/10.1016/j.msea.2017.06.086.

[36] F. Cao, P. Munroe, Z. Zhou, Z. Xie, Medium entropy alloy CoCrNi coatings: enhancing hardness and damage-tolerance through a nanotwinned structuring, Surf. Coat. Technol. 335 (2018) 257–264, https://doi.org/10.1016/j.surfcoat.2017.12.021.

[37] W.-M. Choi, Y.H. Jo, S.S. Sohn, S. Lee, B.-J. Lee, Understanding the physical metallurgy of the CoCrFeMnNi high-entropy alloy: an atomistic simulation study, NPJ. Comput. Mater. 4 (2018) 1–9, https://doi.org/10.1038/s41524-017-0060-9.

[38] Microstructural characterization of ultrafine-grained nickel - Zhilyaev - 2003 - physica status solidi (a)- Wiley Online Library, (n.d.). https://onlinelibrary.wiley.com/doi/abs/10.1002/pssa.200306608 (accessed April 27, 2025).

[39] K. Edalati, Z. Horita, A review on high-pressure torsion (HPT) from 1935 to 1988, Mater. Sci. Eng.: A 652 (2016) 325–352, https://doi.org/10.1016/j.msea.2015.11.074.

[40] A.P. Zhilyaev, T.G. Langdon, Using high-pressure torsion for metal processing: fundamentals and applications, Prog. Mater. Sci. 53 (2008) 893–979, https://doi.org/10.1016/j.pmatsci.2008.03.002.

[41] O. Ciuca, K. Tsuchiya, Y. Yokoyama, Y. Todaka, M. Umemoto, Heterogeneous process of disordering and structural refinement in Ni3Al during severe plastic deformation by high-pressure torsion, Mater. Trans. 51 (2010) 14–22, https://doi.org/10.2320/matertrans.MB200915.

[42] S. Erbel, Mechanical properties and structure of extremely strainhardened copper, Met. Technol. 6 (1979) 482–486, https://doi.org/10.1179/030716979803276363.

[43] O.N. Senkov, F.H. Froes, V.V. Stolyarov, R.Z. Valiev, J. Liu, Microstructure of aluminum-iron alloys subjected to severe plastic deformation, Scr. Mater. 38 (1998) 1511–1516, https://doi.org/10.1016/S1359-6462(98)00073-6.

[44] A.V. Korznikov, O. Dimitrov, G.F. Korznikova, J.P. Dallas, S.R. Idrisova, R. Z. Valiev, F. Faudot, Thermal evolution of high-purity and boron-doped sub-microcrystalline Ni3Al produced by severe plastic deformation, Acta Mater. 47 (1999) 3301–3311, https://doi.org/10.1016/S1359-6454(99)00172-X.

[45] A.P. Zhilyaev, S. Lee, G.V. Nurislamova, R.Z. Valiev, T.G. Langdon, Microhardness and microstructural evolution in pure nickel during high-pressure torsion, Scr. Mater. 44 (2001) 2753–2758, https://doi.org/10.1016/S1359-6462(01)00955-1.

[46] Z. Huang, Y. Ren, D. Luo, Q. Zhou, Y. He, H. Wang, Improved wear resistance of a heterogeneous CoCrNi medium-entropy alloy at cryogenic temperature, Tribol. Lett. 70 (2022), https://doi.org/10.1007/s11249-022-01643-x.

[47] Z.F. Liu, N. Tian, Y.G. Tong, Y.L. Hu, D.Y. Deng, M.J. Zhang, Z.H. Cai, J. Liu, Mechanical performance and deformation behavior of CoCrNi medium-entropy alloy at the atomic scale, Crystals 12 (2022) 753, https://doi.org/10.3390/cryst12060753.

[48] S. Bajpai, B.E. MacDonald, T.J. Rupert, H. Hahn, E.J. Lavernia, D. Apelian, Recent progress in the CoCrNi alloy system, Materialia 24 (2022) 101476, https://doi.org/10.1016/j.mtla.2022.101476.

[49] H. He, M. Naeem, F. Zhang, Y. Zhao, S. Harjo, T. Kawasaki, B. Wang, X. Wu, S. Lan, Z. Wu, W. Yin, Y. Wu, Z. Lu, J.-J. Kai, C.-T. Liu, X.-L. Wang, Stacking fault driven phase transformation in CrCoNi medium entropy alloy, Nano Lett. 21 (2021) 1419–1426, https://doi.org/10.1021/acs.nanolett.0c04244.

[50] H. Fujita, S. Ueda, Stacking faults and f.c.c. (γ) → h.c.p. (ϵ) transformation in 188<math><mtext>18</mtext><mtext>8</mtext></math>-type stainless

steel, Acta Metall. 20 (1972) 759–767, https://doi.org/10.1016/0001-6160(72)90104-6.
[51] E. Gartstein, A. Rabinkin, On the f.c.c. → h.c.p. phase transformation in high manganese-iron alloys, Acta Metall. 27 (1979) 1053–1064, https://doi.org/10.1016/0001-6160(79)90193-7.
[52] L. Remy, A. Pineau, Twinning and strain-induced F.C.C. → H.C.P. transformation in the Fe-Mn-Cr-C system, Mater. Sci. Eng. 28 (1977) 99–107, https://doi.org/10.1016/0025-5416(77)90093-3.
[53] K. Lin, S.-C. Chen, H.-C. Lin, H.-W. Yen, Enhancement in mechanical properties through an FCC-to-HCP phase transformation in an Fe-17.5Mn-10Co-12.5Cr-5Ni-5Si (in at%) medium-entropy alloy, J. Alloys Compd. 898 (2022) 162765, https://doi.org/10.1016/j.jallcom.2021.162765.
[54] L. Remy, Kinetics of strain-induced fcc→hcp martensitic transformation, Met. Trans A 8 (1977) 253–258, https://doi.org/10.1007/BF02661637.
[55] X. Li, L. Chen, Y. Zhao, D. Misra, Influence of manganese content on ε-/α′-martensitic transformation and tensile properties of low-C high-Mn TRIP steels, Mater. Des. 142 (2018), https://doi.org/10.1016/j.matdes.2018.01.026.
[56] N. Pussegoda, W.R. Tyson, P. Wycliffe, G.R. Purdy, Segregation of Manganese during intercritical annealing of dual phase steels, Met. Trans. A 15 A (1984) 1499–1502, https://doi.org/10.1007/BF02648582.
[57] Y. Wang, C. Wu, Y. Liu, M. Tian, X. Lu, X. Su, Insight into the FCC→HCP transformation in Co-rich Co-Cr-Fe-Mn-Ni high-entropy alloys, Metals 13 (2023) 504, https://doi.org/10.3390/met13030504.
[58] F.X. Zhang, S. Zhao, K. Jin, H. Bei, D. Popov, C. Park, J.C. Neuefeind, W.J. Weber, Y. Zhang, Pressure-induced fcc to hcp phase transition in Ni-based high entropy solid solution alloys, Appl. Phys. Lett. 110 (2017) 011902, https://doi.org/10.1063/1.4973627.